Nonlinear saturation of wave packets excited by low-energy electron horseshoe distributions

C. Krafft[1,*] and A. Volokitin[2,3]

[1]*Laboratoire de Physique des Plasmas, Ecole Polytechnique, University Paris–Sud, 91128 Palaiseau Cedex, France*

[2]*Space Research Institute 117997, 84/32 Profsoyuznaya Street, Moscow, Russia*

[3]*IZMIRAN, Pushkov Institute, Troitsk, Moscow, Russia*

(Received 23 January 2013; published 17 May 2013)

Horseshoe distributions are shell-like particle distributions that can arise in space and laboratory plasmas when particle beams propagate into increasing magnetic fields. The present paper studies the stability and the dynamics of wave packets interacting resonantly with electrons presenting low-energy horseshoe or shell-type velocity distributions in a magnetized plasma. The linear instability growth rates are determined as a function of the ratio of the plasma to the cyclotron frequencies, of the velocity and the opening angle of the horseshoe, and of the relative thickness of the shell. The nonlinear stage of the instability is investigated numerically using a symplectic code based on a three-dimensional Hamiltonian model. Simulation results show that the dynamics of the system is mainly governed by wave-particle interactions at Landau and normal cyclotron resonances and that the high-order normal cyclotron resonances play an essential role. Specific features of the dynamics of particles interacting simultaneously with two or more waves at resonances of different natures and orders are discussed, showing that such complex processes determine the main characteristics of the wave spectrum's evolution. Simulations with wave packets presenting quasicontinuous spectra provide a full picture of the relaxation of the horseshoe distribution, revealing two main phases of the evolution: an initial stage of wave energy growth, characterized by a fast filling of the shell, and a second phase of slow damping of the wave energy, accompanied by final adjustments of the electron distribution. The influence of the density inhomogeneity along the horseshoe on the wave-particle dynamics is also discussed.

DOI: 10.1103/PhysRevE.87.053107 PACS number(s): 52.35.Mw, 52.35.Qz, 52.65.−y

I. INTRODUCTION

So-called electron and ion horseshoe distributions are shell-like distributions that can arise in space and laboratory plasmas when particle beams propagate into increasing magnetic fields **B** due to the conservation of the first adiabatic invariant $v_\perp^2/|\mathbf{B}|$, where $v_\perp$ is the velocity of particles in the plane perpendicular to **B**. Such distributions were often observed by satellites and rockets in the earth's magnetosphere [1–6] or in the laboratory [7,8] and are also expected to arise in planetary and stellar magnetospheres where energetic electron fluxes are streaming in inhomogeneous magnetic field configurations [9,10]. In particular, horseshoe distributions are believed to be a free energy source for the auroral kilometric radiation or emissions from other astrophysical objects such as stars, through the mechanism of cyclotron maser instability [11]. The waves excited by such anisotropic distributions $f(v_z, v_\perp)$ (v_z is the velocity of particles along **B**) through shell-type instabilities draw their energy from the positive derivative $\partial f/\partial v_\perp > 0$; such processes are believed to be very efficient and considerably stronger than loss cone-type instabilities [12].

However, horseshoe distributions can also excite waves in quite different situations as, for example, in nonrelativistic and overdense plasmas (with the electron plasma frequency ω_p much higher than the electron cyclotron frequency ω_c) where the conditions favorable for efficient cyclotron maser instability are not met. Recently, observations from the Cluster spacecraft in overdense plasmas of the cusp, mantle, or polar cap have shown that electrostatic and electromagnetic wave emissions above ω_p are associated with the presence of low-energy electron shell-like distributions presenting positive gradients $\partial f/\partial v_\perp > 0$ [13]. In this case, as well as in those mentioned above, the densities of the hot and cold electron populations were supposed to be of the same order. Nevertheless, low-energy horseshoe distributions with densities much smaller than the ambient plasma can also destabilize waves through Landau and cyclotron resonant mechanisms, as shown in this paper. In particular, the gradient $\partial f/\partial v_\perp > 0$ can excite electrostatic waves above ω_p that propagate obliquely to the magnetic field. Such waves, as well as electron cyclotron emissions, both driven by the gradient $\partial f/\partial v_\perp > 0$, have been observed in space and the laboratory together with shell-like distributions (see, e.g., [7,14]) or studied numerically (see, e.g., [15]).

In order to study the dynamics of an electron horseshoe distribution interacting resonantly with electrostatic wave packets, a three-dimensional Hamiltonian model and a symplectic code have been built. The theoretical approach allows us to split the particle velocity distribution into two populations: (i) the nonresonant bulk, i.e., the ambient plasma supporting the wave dispersion, and (ii) the so-called resonant electrons forming the horseshoe, which interact strongly with the waves at different resonance conditions and whose density is much smaller than that of the ambient plasma $n_{res}/n_0 \ll 1$. This situation is worth studying as even low-density shell-type distributions can generate waves of finite amplitudes. Those can be destabilized above ω_p through resonant mechanisms where Landau, normal, and anomalous cyclotron resonances compete. The waves' saturation and the horseshoe relaxation result from complex processes where particle trapping and velocity diffusionlike phenomena occur. In particular, the role of the normal cyclotron resonances and their harmonics in

*catherine.krafft@lpp.polytechnique.fr

the dynamics of the system's, the simultaneous interaction of particles with waves at multiple resonances of different nature or order, and the coupling of waves through their interaction with common groups of particles (note that wave-wave coupling processes are not included in the model) are discussed on the basis of the simulations' results.

The paper is organized as follows. After the determination of the instability growth rates using linear theory and the study of their dependences on the ratio of the plasma to the cyclotron frequency, on the velocity and the opening angle of the horseshoe, and on the relative thickness of the shell (Sec. II), numerical simulations are performed for various horseshoe distributions and wave packets. Section III presents and discusses the wave-particle dynamics successively for the case of a single wave, a few waves, and a wave packet with a quasicontinuous spectrum. Section IV summarizes and states our conclusions. The theoretical model and the numerical code are presented in the Appendix.

II. INSTABILITY OF HORSESHOE DISTRIBUTIONS

The instability growth rate γ_k of a wave of frequency ω_k and wave vector $\mathbf{k}$ destabilized by hot electrons with horseshoe and shell-like velocity distributions f_e can be calculated in the frame of kinetic theory using the well known formula ($\gamma_k \ll \omega_k$)

$$\gamma_k = \frac{\pi k_z}{|k_z|}\left(\frac{\partial \varepsilon_k}{\partial \omega_k}\right)^{-1}\frac{\omega_{pr}^2}{k^2}\sum_{n=-\infty}^{\infty} \times \int_0^\infty d(\pi v_\perp^2) J_n^2\left(\frac{k_\perp v_\perp}{\omega_c}\right) \times \int_{-\infty}^{\infty} dv_z \delta(v_z - v_{zn})\left(\frac{\partial f_e}{\partial v_z} + \frac{n\omega_c}{k_z v_\perp}\frac{\partial f_e}{\partial v_\perp}\right), \quad (1)$$

which is valid for electrostatic waves of any nature in a magnetized plasma (including cyclotron and lower- and upper-hybrid waves). Here

$$v_{zn} = \frac{\omega_k - n\omega_c}{k_z} \quad (2)$$

is the resonant velocity of the wave, with resonance number n, and

$$\varepsilon_k = 1 - \frac{\omega_p^2}{\omega_k^2}\frac{k_z^2}{k^2} - \frac{\omega_p^2}{\omega_k^2 - \omega_c^2}\frac{k_\perp^2}{k^2} - \frac{\omega_{pi}^2}{\omega_k^2} \quad (3)$$

is the plasma dielectric constant of the wave (ions are supposedly not magnetized); $\omega_p$and ω_{pi} are the electron and ion plasma frequencies; ω_c is the electron cyclotron frequency; ω_{pr} is the plasma frequency of the resonant electrons with density n_{res}, $\omega_{pr}^2 = 4\pi n_{res} e^2/m_e$; n_{res} is supposed to be much smaller than the ambient plasma density n_0, $n_{res}/n_0 \ll 1$ (see also the model in the Appendix); k_z and $k_\perp$ are the wave numbers parallel and perpendicular to the constant magnetic field $\mathbf{B}_0$, respectively, with $k_z^2 + k_\perp^2 = k^2$; v_z and $v_\perp$ are the parallel and perpendicular velocities; $f_e(v_z, v_\perp)$ is the velocity distribution of the resonant electrons, normalized as $\int f_e d^3v = 1$; and J_n is the Bessel function of order n.

Further we consider only dense and/or weakly magnetized plasmas with $\omega_p \gg \omega_c$ and upper-hybrid waves, whose instability is developing most rapidly. In this case Eq. (3) provides the approximated dispersion relation (in a cold plasma without thermal effects)

$$\omega_k^2 \simeq \omega_p^2 + \omega_c^2\frac{k_\perp^2}{k_z^2 + k_\perp^2}, \quad (4)$$

with $\partial\varepsilon_k/\partial\omega_k \simeq 2/\omega_k$.

In the general case, for horseshoe and shell distributions, calculations of the growth rates using Eq. (1) require a numerical approach. However, one can get a simple and convenient expression of γ_k for a narrow horseshoe distribution of the form $f_e(v,\theta) = f(v)\Theta(\theta)$; v and θ are the conventional spherical coordinates, where v is the modulus of the velocity $\mathbf{v}$ and θ is the angle between $\mathbf{v}$ and $\mathbf{B}_0$. Passing in Eq. (1) from the cylindrical coordinates $(v_\perp, v_z)$ to the spherical ones using $v_z = v\cos\theta$ and $v_\perp = v\sin\theta$ and integrating on the angle θ we obtain

$$\gamma_k = \pi^2\omega_k\frac{\omega_{pr}^2}{k^2}\sum_{n=-\infty}^{\infty}\int_{|v_{zn}|}^{\infty} dv\frac{k_z\sin\theta_v}{|k_z\sin\theta_v|}J_n^2\left(\frac{k_\perp\sqrt{v^2 - v_{zn}^2}}{\omega_c}\right) \times \left[\sqrt{v^2 - v_{zn}^2}\frac{f(v)}{v}\left(\frac{n\omega_c}{k_z}\frac{v_{zn}}{v^2 - v_{zn}^2} - 1\right)\frac{\partial\Theta(\theta_v)}{\partial\theta_v} + \frac{\partial f(v)}{\partial v}\left(v_{zn} + \frac{n\omega_c}{k_z}\right)\Theta(\theta_v)\right], \quad (5)$$

where $\cos\theta_v = v_{zn}/v$. For an extremely thin horseshoe distribution of velocity v_0, one can use the approximation $f(v) = A_0\delta(v - v_0)$ so that the integration on v provides the normalized growth rate

$$\frac{\gamma_k}{\omega_k} = \pi^2\frac{\omega_{pr}^2}{k^2}A_0\left[\sum_{v_0^2 \geqslant v_{zn}^2}\frac{k_z\sin\theta_{v_0}}{|k_z\sin\theta_{v_0}|}J_n^2(z)\frac{\sqrt{v_0^2 - v_{zn}^2}}{v_0} \times \left(\frac{n\omega_c}{k_z}\frac{v_{zn}}{v_0^2 - v_{zn}^2} - 1\right)\frac{\partial\Theta(\theta_{v_0})}{\partial\theta_{v_0}} - \frac{\omega_k}{k_z}\sum_{v_0^2 \geqslant v_{zn}^2}\frac{\partial}{\partial v_0}\left(\frac{k_z\sin\theta_{v_0}}{|k_z\sin\theta_{v_0}|}\Theta(\theta_{v_0})J_n^2(z)\right)\right], \quad (6)$$

where $z = k_\perp\sqrt{v_0^2 - v_{zn}^2}/\omega_c$ and $\theta_{v_0} = \arcsin(\sqrt{1 - v_{zn}^2/v_0^2})$. If $\Theta(\theta)$ is a smooth function, i.e., $\partial\Theta(\theta_{v_0})/\partial\theta_{v_0}$ tends to zero, the first term in Eq. (6) is small. Let us consider, for example, that $\Theta(\theta) = 1 - H(\theta - \theta_0)$ (H is the Heaviside function and θ_0 can be referred to as the opening angle of the horseshoe). In this case the coefficient $A_0 = [(1 - \cos\theta_0)2\pi v_0^2]^{-1}$ is obtained from $\int f_e(v,\theta)d^3v = 1$. The first term in Eq. (6) is not negligible only at the boundary of the distribution where $\partial\Theta(\theta_{v_0})/\partial\theta_{v_0} \to \delta(v_{zn}/v_0 - \cos\theta_0)$. Thus, excluding the waves with resonant velocities satisfying $v_{zn} = v_0\cos\theta_0$ we get

$$\frac{\gamma_k}{\omega_c} \simeq -\frac{\pi}{2(1 - \cos\theta_0)}\frac{\sin\theta_{v_0}}{|\sin\theta_{v_0}|}\frac{\omega_c}{|k_z|v_0}\frac{\omega_k^2}{\omega_c^2}\frac{\omega_p^2}{\omega_c^2}\frac{n_{res}}{n_0}\frac{k_\perp^2}{k^2} \times \sum_{v_0^2 > v_{zn}^2}\frac{1}{z}\frac{\partial J_n^2(z)}{\partial z}, \quad (7)$$

which in the limit of the shell distribution $\Theta(\theta) = 1$ matches the formula obtained in [15].

Numerical calculations of γ_k using Eqs. (1) and (6) show that the assumption of infinitely thin distributions [providing Eqs. (6) and (7)] are sufficiently accurate if the thickness of the horseshoe (i.e., the scattering of its velocity v_0) is very small, i.e., $\Delta v_0 \simeq \sqrt{\int_0^\infty (v-v_0)^2 f_e(v) dv} \lesssim v_0/40$. The growth rates are calculated using the general formula (1) and the horseshoe distribution with thickness σ [3]:

$$f_e(v,\theta) = A \exp\left[-\left(\frac{v-v_0}{\sigma}\right)^2\right](b\cos\theta + a)^2 H(\theta-\theta_0), \tag{8}$$

where θ_0 is the horseshoe angle. In the figures all results are presented using the dimensionless variables γ_k/ω_c, $k_z\rho$, and $k_\perp\rho$, where $\rho = v_T/\omega_c$ is the Larmor radius and v_T is the electron thermal velocity.

An important feature of the horseshoe instability is that its growth rate γ_k is determined by the sum of several non-negligible resonance terms or, in other words, by the interaction of the wave with several groups of particles of different velocities. This obviously follows from (7) and is confirmed by numerical calculations. Moreover, as a result, the complex dependence of the growth rate on the wave vectors is characterized by the presence of many local maxima of γ_k in the plane $(k_\perp\rho, k_z\rho)$.

The growth rate depends on several parameters characterizing the hot electrons and the plasma. Some of these dependences are simple, such as the proportionality of the maximum growth rate $\gamma_{\max}$ to the ratio of the horseshoe to the ambient plasma densities n_{res}/n_0, resulting from Eq. (1); the others are studied below. Let us first consider how the thickness of the horseshoe affects γ_k and the values of the wave vectors of the most unstable waves. Figures 1(a) and 1(b) show the variation of γ_k/ω_c in the plane $(k_\perp\rho, k_z\rho)$ for (a) a thin and (b) a thick horseshoe distribution, computed using Eq. (1). Note that the calculations of γ_k/ω_c using Eq. (7) (not shown here) are in good agreement with Fig. 1(a). For a thin horseshoe, Fig. 1(a) reveals the existence of several local maxima among which the largest is located near $k_\perp\rho \simeq 1.1$ and $k_z\rho \simeq 1.85$ with $\gamma_{\max}/\omega_c \simeq 0.006$. This maximum is mainly due to the Landau resonance $n = 0$; the normal cyclotron resonance harmonics $n > 1$, even if they also contribute to the wave growth in the same wave-number ranges as the main resonance $n = 1$, are responsible for instability in the lower part of the $(k_\perp\rho, k_z\rho)$ plane ($k_z\rho \lesssim 1.6$); the anomalous cyclotron harmonics $n < 0$ also contribute to growth, but at higher values of k_z [not visible in Figs. 1(a) and 1(b)]. Comparing Figs. 1(a) and 1(b), one observes that when the thickness of the shell is larger, $\gamma_{\max}$ is smaller [$\gamma_{\max}/\omega_c \simeq 0.0023$ near $k_\perp\rho \simeq 2.5$ and $k_z\rho \simeq 0.3$ for Fig. 1(b)]; however, the maximum growth rate is not due to the Landau resonance, but mainly to the higher-order resonances $n > 1$, whereas the islands where $\gamma_k > 0$ in Fig. 1(a) (corresponding to $n \geqslant 0$) have merged. Thus, for a larger thickness, $\gamma_{\max}$ is reduced, but the energy extraction at the normal cyclotron resonances is stronger than at the Landau resonance. Moreover, the differences between Figs. 1(a) and 1(b) make evident that Eq. (7) is not applicable for $\sigma \gtrsim v_0/40$. Finally, the dependence of $\gamma_{\max}/\omega_c$ on σ is well described by the power law

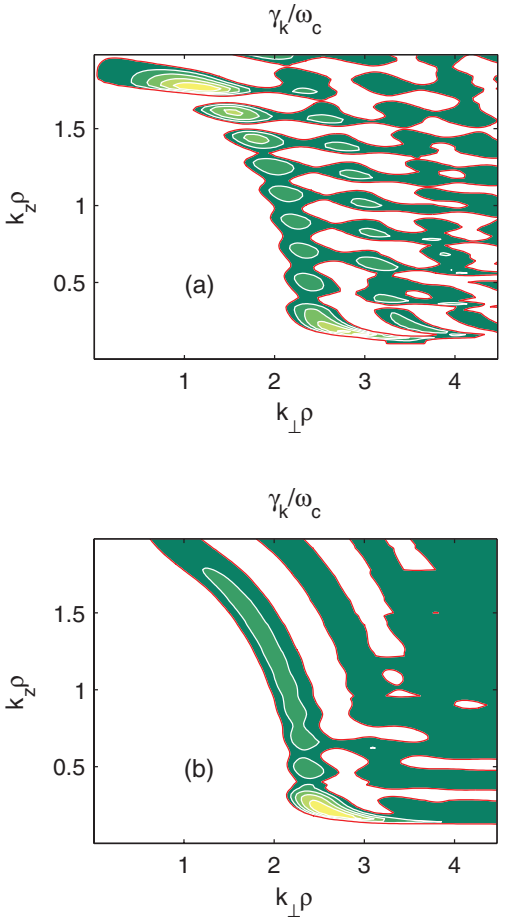

FIG. 1. (Color online) Variation of the normalized growth rate γ_k/ω_c in the plane $(k_\perp\rho, k_z\rho)$ for (a) a thin horseshoe and (b) a thick horseshoe, calculated using Eq. (1), for $\omega_p/\omega_c = 8.5$, $v_0 = 5$, $\theta_0 = 137^\circ$, $n_{res}/n_0 = 0.0001$, $a = 1$, and $b = 0$, and (a) $\sigma \simeq v_0/40$ and (b) $\sigma \simeq v_0/10$. All resonances are taken into account in (1), i.e., $n < 0$, $n = 0$, and $n > 0$. The regions of instability ($\gamma_k > 0$) and the corresponding isocontours are represented by gray (colored) surfaces and white lines, respectively (the red contours visible online are the boundary lines where $\gamma_k = 0$). The maximum growth rate is located near (a) $(k_\perp\rho \simeq 1.1, k_z\rho \simeq 1.85)$ and (b) $(k_\perp\rho \simeq 2.5, k_z\rho \simeq 0.3)$.

$\gamma_{\max}/\omega_c \propto (\sigma/v_0)^{-0.5}$ for $\sigma \lesssim v_0/10$; then, when increasing σ, the decrease of $\gamma_{\max}$ becomes faster.

The necessity to take into account the contributions of higher-order resonances is illustrated by Fig. 2, where $\gamma_{\max}/\omega_c$ is calculated as a function of the opening angle θ_0 using Eq. (1), with the following resonances included: (i) $n = 0$ only (stars), (ii) $n = 1$ only (circles), and (iii) all resonances (triangles); note that the contribution of the resonances $n < 0$ is negligible in the regions of the $(k_\perp\rho, k_z\rho)$ plane considered. The following important point has to be stressed: For (i) and (ii) the wave number $k_{z\max}\rho$ corresponding to $\gamma_{\max}$ is around 0.6, whereas for (iii), $k_{z\max}\rho \simeq 0.04$; the higher-order resonances shift $\gamma_{\max}$ to significantly lower values of k_z. One can see that the growth rates $\gamma_{\max}$ are the largest at small angles ($\theta_0 \lesssim 50^\circ$) and decrease monotonically as a function of θ_0 at bigger angles. The Landau resonance $n = 0$ contribution overcomes that of the normal cyclotron resonances only at very small angles $\theta_0 \lesssim 20^\circ$. However, normal cyclotron resonances are

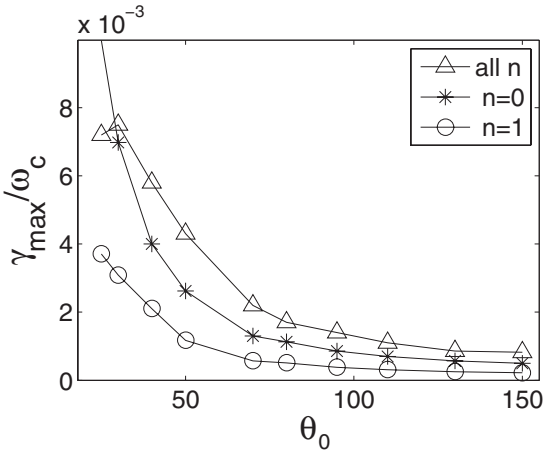

FIG. 2. Variation of the maximum normalized growth rate $\gamma_{\max}/\omega_c$ as a function of the horseshoe angle θ_0 (in degrees) for the following resonances: (i) $n = 0$ only (stars), (ii) $n = 1$ only (circles), and (iii) all resonances n (triangles). For (i) and (ii), $k_{z\max}\rho \simeq 0.6$ and for (iii), $k_{z\max}\rho \simeq 0.04$. The main parameters are $\omega_p/\omega_c = 3$, $v_0 = 5$, $\sigma \simeq v_0/20$, $b = 0$, $a = 1$, and $n_{res}/n_0 = 0.0001$.

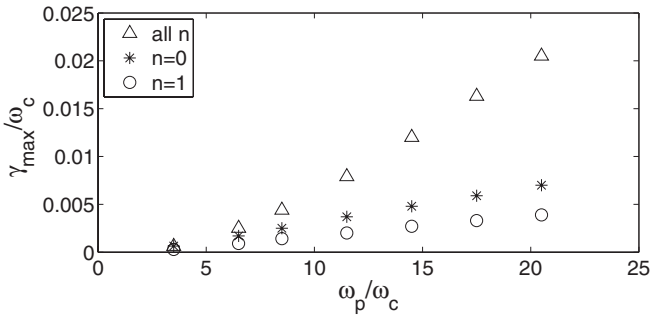

FIG. 3. Variation of the maximum normalized growth rate $\gamma_{\max}/\omega_c$ as a function of the plasma ratio ω_p/ω_c for the resonances (i) $n = 0$ only (stars), (ii) $n = 1$ only (circles), and (iii) all resonances n (triangles). Note that for (iii), $k_{z\max}\rho \simeq 0.02$, whereas for (i) and (ii), $k_{z\max}\rho \gtrsim 0.6$. This figure should be examined together with Table I. The main parameters are $v_0 = 5$, $\sigma \simeq v_0/20$, $b = 0$, $a = 1$, and $n_{res}/n_0 = 0.0001$.

responsible for the main growth of waves for almost all angles $\theta_0 \gtrsim 20^\circ$ and the contribution of the higher harmonics $n > 1$, which is almost always larger than that of the fundamental $n = 1$, is shown to be essential. One should note that if the maximum growth rates correspond to different domains of wave numbers for each kind of resonance ($k_{z\max}$ decreases when n increases, contrary to $k_{\perp\max}$), waves destabilized by Landau and normal cyclotron resonances present rather close phase velocities (e.g., $\Delta v_{zn}/v_{zn} \simeq 0.1$, $v_{zn} \simeq 4$) and thus compete together when interacting with the same group of particles; this feature has important consequences for what concerns the wave-particle evolution, as we will see below.

Calculations show that the dependence of $\gamma_{\max}$ on the horseshoe velocity $v_0 \gg v_T$ is weak (not shown here). The contribution of the normal cyclotron resonances $n \geqslant 1$ to $\gamma_{\max}/\omega_c$ does not depend on v_0, but the position of $\gamma_{\max}$ in the plane $(k_\perp\rho, k_z\rho)$ is sensitive to v_0 as the corresponding $k_{z\max}$ and $k_{\perp\max}$ are proportional to v_0^{-1}. However, the contribution of the Landau resonance $n = 0$ to $\gamma_{\max}$ is proportional to v_0.

Another important parameter that controls the instability is the ratio ω_p/ω_c of the plasma to the cyclotron frequency. Figure 3 shows the variation of $\gamma_{\max}/\omega_c$ with ω_p/ω_c when the following resonances are included: (i) $n = 0$ only (stars), (ii) $n = 1$ only (circles), and (iii) all resonances (triangles); one observes the growth of $\gamma_{\max}$ with ω_p/ω_c as well as the essential role of the higher-order cyclotron resonances [in particular at high ω_p/ω_c]. As revealed by Figs. 1 and 2, two main regions of maximum local growth rate exist, at small $k_z\rho$ and at larger $k_z\rho$, which are markedly separated from each other, so the parallel wavelengths of the unstable waves in these two areas differ significantly. Table I (complementary to Fig. 3) summarizes the values of $\gamma_{\max}/\omega_c$ and the corresponding wave numbers $k_{z\max}\rho$ and $k_{\perp\max}\rho$ as a function of ω_p/ω_c for these two instability regions [the subscript 1 refers to the region at small $k_z\rho$ and the subscript 2 to the rest of the $(k_\perp\rho, k_z\rho)$ plane]. One can see that for small ω_p/ω_c the values of $(\gamma_{\max}/\omega_c)_1$ and $(\gamma_{\max}/\omega_c)_2$ are close, but for $\omega_p/\omega_c \gtrsim 8.5$ the difference between them begins to rise sharply, reaching a ratio $(\gamma_{\max}/\omega_c)_1/(\gamma_{\max}/\omega_c)_2 \simeq 5$ at $\omega_p/\omega_c = 20.5$.

Discussing the behavior of the instability at small k_z, note the specific case of the so-called double plasma resonance condition, i.e., when $\omega_k \simeq n\omega_c$; then, as $k_z = (\omega_k - n\omega_c)/v_{zn} \to 0$, the wave with the largest parallel wavelength can be excited and interact with the hot electrons at the finite resonant velocity v_{zn}. For upper-hybrid waves, this condition occurs at $\omega_p \simeq n\omega_c$, i.e., $n = integer$ (ω_p/ω_c); then the contribution of the corresponding term in Eq. (7) becomes dominant and

TABLE I. Normalized values of the maximum growth rates $\gamma_{\max}/\omega_c$ and corresponding wave numbers $k_{z\max}\rho$ and $k_{\perp\max}\rho$ as a function of ω_p/ω_c for the two instability regions; the subscript 1 refers to the domain at small $k_z\rho$ (see also Fig. 1) and the subscript 2 to the rest of the $(k_\perp\rho, k_z\rho)$ plane. The parameters are the same as in Fig. 3.

ω_p/ω_c	$(\gamma_{\max}/\omega_c)_1$	$(\gamma_{\max}/\omega_c)_2$	$(k_{z\max}\rho)_1$	$(k_{z\max}\rho)_2$	$(k_{\perp\max}\rho)_1$	$(k_{\perp\max}\rho)_2$
3.5	6.1×10^{-4}	7.5×10^{-4}	0.18	0.77	1.43	0.75
6.5	0.0025	0.0021	0.18	1.39	2.23	0.97
8.5	0.0044	0.0028	0.18	1.79	2.76	1.12
11.5	0.0079	0.0033	0.18	2.37	3.53	1.37
14.5	0.012	0.0036	0.18	2.95	4.31	1.64
17.5	0.0163	0.004	0.18	3.16	5.08	2.65
20.5	0.0205	0.0046	0.17	3.18	5.08	2.65

the growth rate can be written as

$$\gamma_k \simeq -\frac{\pi}{(1-\cos\theta_0)}\frac{\omega_k^2}{\left|\omega_p\left(1+\frac{1}{2n^2}\frac{k_\perp^2}{k_z^2+k_\perp^2}\right)-n\omega_c\right|} \times \frac{|v_{zn}|}{v_0}\frac{n_{res}}{n_0}\frac{\omega_p^2}{\omega_c^2}\frac{k_\perp^2}{k^2}\frac{\partial J_n^2(z_n)}{\partial z_n^2}, \quad (9)$$

where the wave vectors of the most unstable waves have to be determined using the double resonance condition as well as $z_n = k_\perp\sqrt{v_0^2 - v_{nz}^2}/\omega_c = z_{n\max}$ [at $z_{n\max}$ the maximum of $\partial J_n^2(z_n)/\partial z_n^2$ is reached]. The presence of a singularity at $\omega_p/\omega_c = n^3/(n^2+1/2)$ ($\omega_p/\omega_c > 1/2$) in Eq. (9) indicates that the conditions for kinetic instability are broken. In fact, under the conditions of double resonance, upper-hybrid waves with $k_z \to 0$ become unstable (see [16,17] and Chap. 8.4 of [18]) and this instability is hydrodynamic. Note that the exact consideration of this case requires the inclusion of relativistic effects [19]. In view of the above, the study of the wave instability near the double resonance is beyond the scope of this paper and requires a separate consideration. In particular, it should be noted that in Fig. 3 it is not possible to interpolate the dependence of $\gamma_{\max}/\omega_c$ on ω_p/ω_c to waves with frequencies corresponding to the double resonance condition.

In conclusion, horseshoe distributions can destabilize upper-hybrid waves in large ($k_\perp\rho$,$k_z\rho$) domains, with growth rates resulting from a competition between the resonances $n = 0,1$ and the higher-order normal cyclotron resonances $n > 1$. Some interesting features of the instability have been studied, mainly the dependence of the maximum growth rates on the horseshoe angle, thickness, and velocity as well as on the plasma ratio ω_p/ω_c. Note that if the contribution of the bulk particles of density n_0 (described by a Maxwellian of thermal velocity v_T) to the growth rates is taken into account (which is not the case here in the frame of our approach), γ_k is reduced but not crucially diminished: The cold Maxwellian bulk does not suppress the horseshoe instability if $v_0 \gg \Delta v_0, v_T$.

III. NUMERICAL SIMULATIONS

The numerical simulations are based on a three-dimensional theoretical model that describes the quasilinear evolution of electrostatic waves interacting resonantly with particles in a magnetized plasma (see the Appendix and [20,21]). This model can be considered as an alternative to the so-called quasilinear theory of weak turbulence usually applied to study the nonlinear stage of interactions between waves and particles. Such an approach of the wave-particle interaction was developed and used in previous works, including ours, and its efficiency and validity have been proved for different physical situations by comparing its results with experimental observations as well as with numerical simulations based on other methods.

We investigate here the nonlinear dynamics of electrostatic upper-hybrid waves interacting with a flow of electrons presenting a horseshoe-type velocity distribution. Assuming that the density n_{res} of the hot electrons is small with respect to that of the ambient plasma density, we take into account only the interactions of the resonant particles with the waves, i.e., for which the resonance conditions $\omega_k - n\omega_c - k_z v_z = 0$ are fulfilled. We suppose also that the waves' amplitudes are small, even at well developed nonlinear stages; thus it is possible to neglect the nonlinear processes of wave-wave coupling. All results are presented below in a dimensionless form: The velocities and the waves' electric fields are normalized by the thermal velocity ($v/v_T \to v$) and the thermal energy ($|E_k|^2/16\pi n_0 T_e \to |E_k|^2$, T_e is the electron temperature of the bulk), respectively.

A. Dynamics of the resonant wave-particle interaction

Let us first consider the case of a single wave, which can be used to present and illustrate some important features of the resonant wave-particle interactions. We choose a wave ($k_z\rho = 0.54$ and $k_\perp\rho = 0.99$) and a horseshoe distribution ($v_0 = 5$, $\theta_0 = 137^\circ$, $\sigma \simeq v_0/20$, $a = 1$, and $b = 0$) in a such way that the particles can interact with the wave only at the normal cyclotron resonance $n = 1$ and its harmonics ($n = 2$–5), the resonant velocities v_{zn} corresponding to the other resonance numbers n verifying $|v_{zn}| > v_0$ (see also Fig. 5). Figure 4 shows the time dependence of the electric field energy density $W_k = |E_k|^2$ and the corresponding variation of the total kinetic energy density of the particles, $\mathcal{E} = (n_{res}/n_0)\sum_p(v_p^2 - v_{p0}^2) \propto \langle\Delta v^2\rangle$; the inset presents $|E_k|^2(t)$ on a logarithmic scale for $\omega_c t/2\pi < 140$. The growth rate of the wave instability, obtained by the simulation in the linear stage of the evolution, is $\gamma_k/\omega_c \simeq 0.057$ (see the inset), which is consistent with the value $\gamma_k/\omega_c \simeq 0.06$ calculated using Eqs. (1) and (7). The balance between the kinetic energy and the wave energy holds with high accuracy, which is also the case for all of the calculations discussed below. The parallel and the perpendicular kinetic energy densities of the particles, i.e., $\mathcal{E}_z \propto \langle\Delta v_z^2\rangle$ and $\mathcal{E}_\perp \propto \langle\Delta v_\perp^2\rangle$, are decreasing as $\mathcal{E}$ (not shown here): The particles lose energy along and

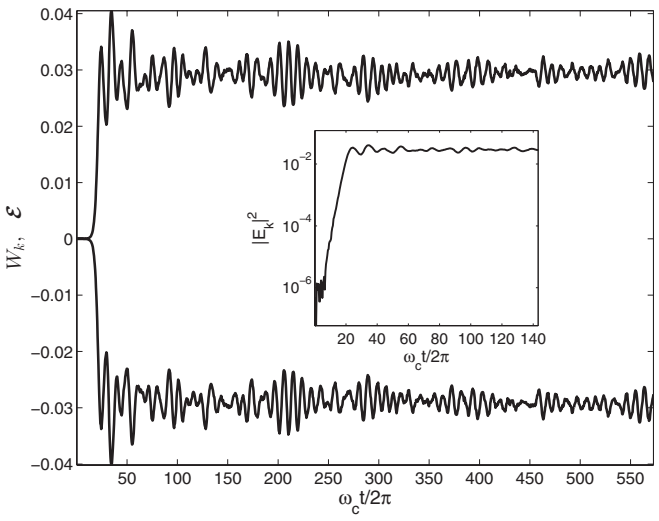

FIG. 4. Case of a single wave: variation with the normalized time $\omega_c t/2\pi$ of the wave energy and the total kinetic energy densities $W_k = |E_k|^2$ (upper curve) and $\mathcal{E} = (n_{res}/n_0)\sum_p(v_p^2 - v_{p0}^2)$ (lower curve), respectively, in arbitrary units. The inset shows the time variation of $|E_k|^2$ on a logarithmic scale for $\omega_c t/2\pi < 140$. The main parameters are $\omega_p/\omega_c = 3$, $v_0 = 5$, $\theta_0 = 137^\circ$, $\sigma \simeq v_0/20$, $n_{res}/n_0 = 0.023$, $a = 1$, and $b = 0$.

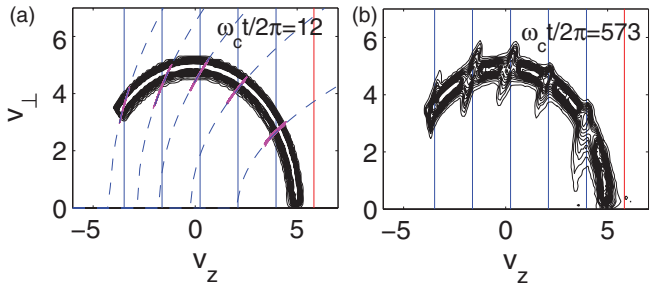

FIG. 5. (Color online) Isocontours of the particle distribution in the plane $(v_z, v_\perp)$ for two moments of time at the initial and final stages of the simulation: (a) $\omega_c t/2\pi = 12$ and (b) $\omega_c t/2\pi = 573$, respectively. The vertical lines mark the positions of the resonant velocities v_{zn} for $n = 0$ (red) and $n = 1$–5 (blue), i.e., $v_{z0} \simeq 5.82$, $v_{z1} \simeq 3.98$, $v_{z2} = 2.13$, $v_{z3} = 0.24$, $v_{z4} = -1.62$, and $v_{z5} = -3.48$. (a) The invariants of the motion, i.e., the lines $n\omega_c v_z/k_z - v_\perp^2/2 \simeq \mathcal{C}$ (10), are shown for $n = 1$–5 [dashed (blue) curves] as well as the projections of five test particles trajectories [thick gray (pink) segments on the dashed lines]. (b) The five groups of particles involved in the interaction at each resonance $n = 1$–5 form structures elongated along the conservation lines. The parameters are the same as in Fig. 4.

across the magnetic field, transferring it to the wave that grows exponentially and then saturates by particle trapping near $\omega_c t/2\pi \simeq 20$, reaching $|E_k^2|_s \simeq 0.035$.

Figures 5(a) and 5(b) show the isocontours of the particle distribution function in the plane $(v_z, v_\perp)$ for two moments of time, at (a) the initial and (b) the final stages of the simulation. The vertical lines mark the positions of the resonant velocities v_{zn} for $n = 0$–5. One can see that the wave interacts with different groups of particles and that the distribution is essentially modified in the vicinity of the velocities v_{zn} for $n = 1$–5. The role of the higher-order harmonics $n > 1$ of the normal cyclotron resonance $n = 1$ appears to be determinant, in the linear stage (as expected from the above linear calculations) as well as in the nonlinear stage. Each group of particles interacting with the wave at different n diffuses to perpendicular velocities lower as well as higher than v_0 and is trapped by the wave, the electrons performing the vibrational motion along the conservation lines

$$\frac{n\omega_c}{k_z} v_z - \frac{v_\perp^2}{2} \simeq \mathcal{C}, \tag{10}$$

moving both below and above their initial perpendicular velocity ($\mathcal{C}$ is a constant). This behavior is typical of wave-particle interaction at cyclotron resonances (see [20–22]) and corresponds to the invariant motion of particles in a wave field of quasiconstant amplitude [23]. Note that for normal cyclotron resonances $n \geqslant 1$, the slope $\Delta v_\perp/\Delta v_z = n\omega_c/k_z v_\perp$ of the line (10) at $v_\perp$ and the wave number k_z have the same sign. In Fig. 5(a) the projections of five test particle trajectories on the plane $(v_z, v_\perp)$ are shown, each forming a tight line with slope $n\omega_c/k_z v_\perp$ at $v_\perp$.

Finally, the variation of the wave energy density $|E_k|^2_{\max}$ at saturation (first maximum) and the time T_s at which it occurs have been calculated as a function of the density ratio n_{res}/n_0 for the parameters of Figs. 4 and 5. One finds that $|E_k|^2_{\max} \propto (n_{res}/n_0)^3$, whereas T_s scales as $(n_{res}/n_0)^2$ below some threshold ($n_{res}/n_0 \simeq 0.002$) and is exponentially decreasing above it. Such scaling of $|E_k|^2_{\max}$ with (n_{res}/n_0) was also observed for loss cone instabilities destabilized at normal cyclotron resonances [21,22].

If there are a few or many waves, the situation changes dramatically. Indeed, due to the modifications of the particle distribution during the time evolution, the waves that were stable initially can be destabilized after some time and begin to grow. Moreover, their amplitude can exceed that of the waves dominating in the initial stage of the relaxation. In addition, the same group of particles can be simultaneously in resonance with two or more waves, so the trajectories of these electrons become more complex than what we described above. As a result, particle diffusion in velocity space may increase, which contributes to a faster and stronger relaxation of the electron distribution. To analyze this problem, let us consider as a first step the case of four waves. The selected waves have close frequencies $\omega_k = [3.115, 3.123, 3.129, 3.126]$ and their wave numbers are $k_z\rho = [0.625, -0.650, 0.537, 0.562]$ and $k_\perp\rho = [0.913, 1.076, 0.990, 0.990]$; note that the parallel wave number of the second wave is pointing in the direction opposite to the other ones (as well as to the ambient magnetic field), i.e., $k_z\rho(2) \equiv k_{z2}\rho < 0$. The corresponding resonant velocities are the following: (i) for $n = 0$ (Landau resonance), $v_{z0} = [4.984, -4.805, 5.821, 5.558]$; (ii) for $n = -1$ (anomalous cyclotron resonance), $v_{z(-1)} = [6.584, -6.343, 7.682, 7.336]$; and (iii) for $n = 1$ (normal cyclotron resonance), $v_{z1} = [3.384, -3.266, 3.961, 3.780]$. Below we attribute a number to each wave, which corresponds to its rank in the lists of values given for ω_k, $k_z\rho$, $k_\perp\rho$, and v_{zn}; for example, the third wave has a Landau resonant velocity $v_{z0}(3) = 5.821$. The initial particle distribution and the plasma parameters are the same as in Figs. 4 and 5 (single-wave case). Note that for all the waves, there are no particles interacting at $n = -1$ resonances (as $v_0 < |v_{z(-1)}|$) and only the fourth wave can interact with particles at the Landau resonance (at $v_{z0} = 5.558$). Owing to the nearness of the frequencies and the wave vectors, most of the higher-order cyclotron resonant velocities v_{zn} with $n > 1$ verify $|v_{zn}| < v_0$, so it is possible to study the dynamics of the particles interacting with them.

Figure 6 shows the variation with time $\omega_c t/2\pi$ of (a) the energy density $|E_k|^2$ of each wave and (b) the total energy density $W = \sum_k |E_k|^2$ of the waves (upper curve) as well as the total, the parallel, and the perpendicular kinetic energy densities of the particles, $\mathcal{E}$, $\mathcal{E}_z$, and $\mathcal{E}_\perp$ (lower, dashed, and thin curves, respectively). The insets in both panels present the time evolution of the same quantities, but for the initial stage of the simulation when $\omega_c t/2\pi \lesssim 120$. In contrast to the single-wave case discussed above, attention is drawn to the nonmonotonic evolution of the energy densities of the waves [Fig. 6(a)] and the particles [Fig. 6(b)]. The second and third waves grow more quickly than the others and reach saturation at first near $\omega_c t/2\pi \simeq 50$ [see the inset of Fig. 6(a)]; then the second wave's amplitude drops to almost vanish, whereas the energy of the third one continues to grow, but not exponentially. Thus there is a redistribution of energy between these waves during their interactions with one or more groups of common resonant particles. Meanwhile, the fourth wave grows slowly and reaches its first saturation at a lower level around $\omega_c t/2\pi \simeq 150$. From this stage of the evolution

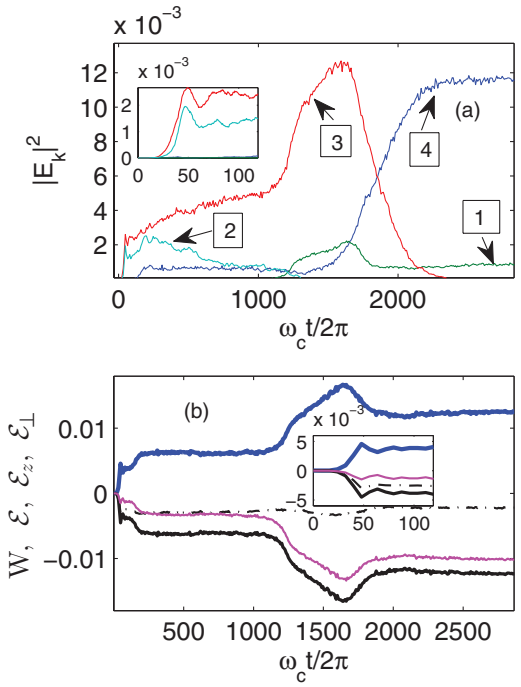

FIG. 6. (Color online) Case of four waves: (a) variation with time $\omega_c t/2\pi$ of the energy density $W_k = |E_k|^2$ of each wave, which is labeled by its number (see also the text), and (b) variation with time of the total energy density $W = \sum_k |E_k|^2$ of the waves [upper (blue) curve] as well as the total [lower black curve], the parallel (upper middle dashed curve), and the perpendicular [lower middle gray (pink) curve] kinetic energy densities of the particles, $\mathcal{E}$, $\mathcal{E}_z$, and $\mathcal{E}_\perp$, respectively. The insets in (a) and (b) present the same time evolutions, but for the initial stage of the simulation when $\omega_c t/2\pi \lesssim 120$. The main parameters are $\omega_p/\omega_c = 3$, $v_0 = 5$, $\theta_0 = 137^\circ$, $\sigma \simeq v_0/20$, $n_{res}/n_0 = 0.008$, $a = 1$, and $b = 0$.

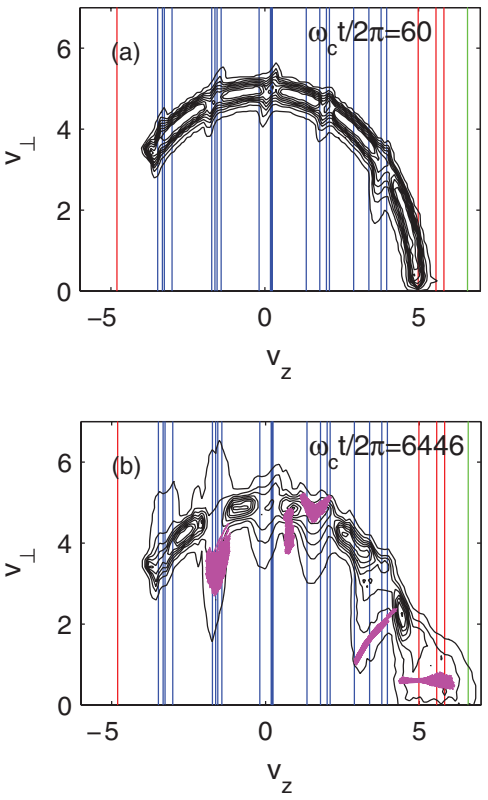

FIG. 7. (Color online) Case of four waves: isocontours of the horseshoe distribution in the plane $(v_z, v_\perp)$ for two moments of time (a) $\omega_c t/2\pi \simeq 60$ and (b) $\omega_c t/2\pi \simeq 6446$. The resonant velocities of the high-order normal cyclotron resonances $n = 2$–5 are the following (v_{z0}, v_{z1}, and $v_{z(-1)}$ are given in the text): $v_{z2} = [1.784, -1.728, 2.10, 2.003]$, $v_{z3} = [0.184, -0.189, 0.240, 0.225]$, $v_{z4} = [-1.416, 1.349, -1.621, -1.553]$, $v_{z5} = [-3.016, 2.888, -3.481, -3.331]$; all these velocities are represented by vertical lines in (a) and (b), except for most of the velocities $v_{z(-|n|)}$ at the anomalous cyclotron resonances, which are beyond the domain of the particles' velocities (blue, red, and green lines for $v_{z(|n|)}$, v_{z0}, and $v_{z(-|n|)}$, respectively). In (b) the projections of five test particle trajectories are superimposed on the distribution, forming gray (pink) areas (see Fig. 8 for enlarged views). The parameters are the same as in Fig. 6.

up to $\omega_c t/2\pi \lesssim 1000$, the variations of the parallel and the perpendicular kinetic energies are roughly the same and vary only slightly.

Further, between $\omega_c t/2\pi \simeq 1000$ and 1600, the third wave's amplitude increases dramatically, whereas a simultaneous energy growth of the fourth and first waves occurs. Note that these waves have a common group of resonant particles in the vicinity of $v_z \simeq -3.3$ at $v_{z5}(1,3,4) = \{-3.016, -3.481, -3.331\}$ ($n = 5$) [whereas $v_{z1}(2) = -3.266$ ($n = 1$)] as well as near $v_z \simeq -1.7$ at $v_{z4}(1,3,4) = \{-1.416, -1.621, -1.553\}$ ($n = 4$) [whereas $v_{z2}(2) = -1.728$ ($n = 2$)]. The simultaneous increase of energy of these three waves is partly due to the expansion of the total width of resonance and, consequently, to the increase of the number of particles entering in the energy exchange with them; however, a more important effect is apparently the change in nature of the particles' motion, which interact at multiple resonances with several waves (see below). Note that there is a sharp decrease of the perpendicular kinetic energy $\mathcal{E}_\perp$, while the energy of the parallel particle motion presents only small variations. Then, near $\omega_c t/2\pi \simeq 1600$ the dynamics of the waves again changes dramatically: The fourth wave continues to grow and its growth is accompanied by a clear decrease of the third wave's energy. In this process, the perpendicular energy of the particles increases markedly, which is conditioned by the almost complete attenuation of the third wave. Next a steady state is set in which almost all the field energy is concentrated in the fourth wave.

All these variations of the waves' and particles' energies are due to the complex dynamics of particles interacting simultaneously at different resonances n with several waves. To illustrate this, Fig. 7(a) presents the isocontours of the electron distribution in the plane $(v_z, v_\perp)$ at time $\omega_c t/2\pi \simeq 60$, when the second and third waves have reached their first saturation level [Fig. 6(a)]. Figure 7(b) shows the horseshoe distribution at a further time $\omega_c t/2\pi \simeq 6446$, when the asymptotic steady state is installed, superposed on the projections of five test particle trajectories. One observes that, along with the particles oscillating along the invariant lines (10), some trajectories present amazing features. Let us examine them in more detail on the enlarged views of Fig. 8.

Figure 8(c) shows the trajectory of a test particle oscillating under the influence of waves 1, 3, and 4, interacting

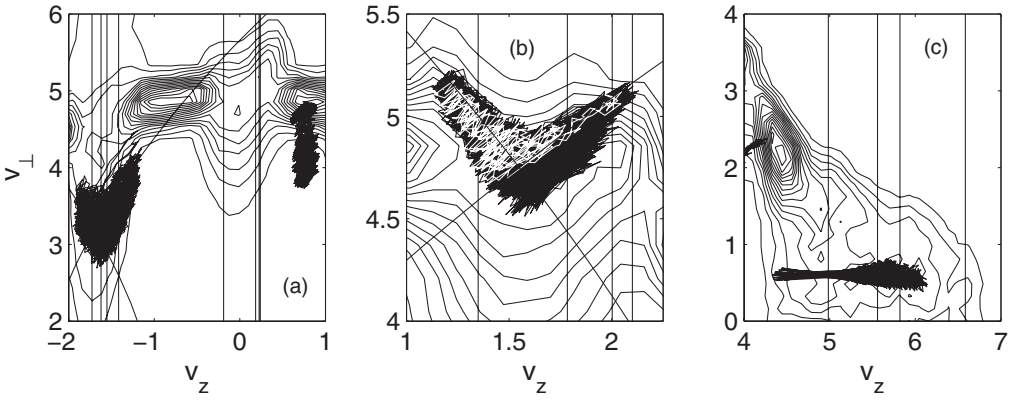

FIG. 8. Case of four waves: enlarged views of the four trajectories of Fig. 7(a). (a)–(c) Superposition in the plane $(v_z, v_\perp)$ of (i) the isocontours of the horseshoe distribution, (ii) the vertical lines representing the resonant velocities, (iii) the invariant lines of motion for the main resonances, which are crossing here (oblique lines), and (iv) the projections of four test particles' trajectories, forming black areas. (a) and (b) The test electrons interact at high-order normal cyclotron resonances $n > 1$ with the waves. (a) The left-hand-side trajectory crosses the resonant velocities $v_{z2}(2) \simeq -1.727$ $(n = 2)$ as well as $v_{z4}(1) \simeq -1.416$, $v_{z4}(3) \simeq -1.620$, and $v_{z4}(4) \simeq -1.553$ $(n = 4)$; the invariant (oblique) lines correspond to $n = 2$ for wave 2 and $n = 4$ for wave 1; the right-hand-side trajectory forming a vertical structure near $v_z \simeq 0.7$ is a beating between the waves 1 and 2. (b) The trajectory crosses the resonant velocities $v_{z2}(1) \simeq 1.784$ $(n = 2)$ and $v_{z4}(2) \simeq 1.349$ $(n = 4)$; the invariant oblique lines correspond to $n = 2$ for wave 1 and $n = 4$ for wave 2. Above the projection of the trajectory drawn up to the asymptotic time (black area), we have superimposed the same trajectory up to a shorter time period (white area). (c) Interaction of a test particle at the three Landau resonances of waves 1, 3, and 4, $v_{z0}(1,3,4) = \{4.984, 5.821, 5.558\}$; the conservation line of the motion is $v_\perp \simeq \mathcal{C}$. The parameters are the same as in Fig. 6.

with them at their Landau resonant velocities $v_{z0}(1,3,4) = \{4.984, 5.821, 5.558\}$; as $n = 0$ the invariant of the motion is $v_\perp \simeq \mathcal{C}$ [Eq. (10)]. A more detailed examination of the time variation of the parallel velocity $v_z(t)$ reveals that the particle jumps from one resonance to another, crossing the common domain of resonance of the different waves, as previously studied in [24–26]. The V-shaped projections of the trajectories presented in Figs. 8(a) and 8(b) correspond to the motion of particles interacting simultaneously at normal cyclotron resonances of different orders with several waves. In particular, the electron in Fig. 8(b) interacts simultaneously with wave 1 at $v_{z2}(1) \simeq (\omega_{k1} + 2\omega_c)/k_{z1} \simeq 1.784$ $(n = 2)$ and with wave 2 at $v_{z4}(2) \simeq (\omega_{k2} + 4\omega_c)/k_{z2} \simeq 1.349$ $(n = 4)$; the corresponding invariant lines of motion (10) intersect due to the different signs of k_{z1} and k_{z2} [see the solid oblique lines in Fig. 8(b)]. Above the projection of the trajectory calculated up to the asymptotic time (forming the black area), we have superimposed the same trajectory limited to a shorter time (forming the white area); one can see that the motion of the particle is composed of random fluctuations around the invariant lines of each resonance. During the full time of the simulation, these fluctuations cumulate and, as a result, the trajectory fills a V-shaped region of finite thickness. The same features can be observed in Fig. 8(a), where the test particle oscillates over four resonances (left trajectory), interacting at normal cyclotron resonances of different orders, i.e., at $v_{z2}(2) \simeq -1.727$ $(n = 2)$, as well as at $v_{z4}(1) \simeq -1.416$, $v_{z4}(3) \simeq -1.620$, and $v_{z4}(4) \simeq -1.553$ $(n = 4)$; the two invariant lines corresponding to (i) wave 2 at $n = 2$ and (ii) the three other waves at $n = 4$ (which have very close invariant lines) are shown (oblique lines).

The projection of the trajectory forming a vertical bar on the right of Fig. 8(a) near $v_z \simeq 0.7$ results from the resonant interaction of the test particle with the beat of two waves. Indeed, no resonant velocity of any wave is present near $v_z \simeq 0.7$, but the resonant velocity of the beating between waves 1 and 2, given by $v_{beat} = (\omega_{k1} - \omega_{k2} - s\omega_c)/(k_{z1} - k_{z2}) \simeq s\omega_c/(k_{z1} - k_{z2}) \simeq 0.74$ for $s = 1$, is close to the particle's velocity. The resonant velocities corresponding to the beatings between the second wave and the third and fourth waves are also close to this velocity range. Since the interaction of electrons with the beatings of waves is weaker than with the waves themselves (as beatings result from nonlinear processes of higher order), the variation of the particle velocity during a single oscillation is small; however, as a result of many oscillations, the particle diffuses along the vertical path $v_z \simeq v_{beat}$. In this case we can conclude that, due to the relative weakness of the interaction and the small number of cases encountered, the interaction of particles with beatings of waves does not play any significant role in the evolution of the particle distribution and the dynamics of the waves.

B. Horseshoe filling and wave energy evolution

Limitations of computer resources do not allow, in the framework of our model, us to perform simulations with numbers of waves exceeding $N_w = 500$–1000; thus the question arises as to how adequately a real system with a continuous spectrum of waves can be described. With no definitive answer to this question, we note that if the waves are distributed densely enough, that is, if each particle can be simultaneously in resonance with several waves (linear resonance overlap) and if the distribution of the wave vectors $\mathbf{k}$ does not present any artificial regularity, the calculation results depend only quantitatively and not strongly on how the waves are distributed in the $\mathbf{k}$ space. This was shown in our previous

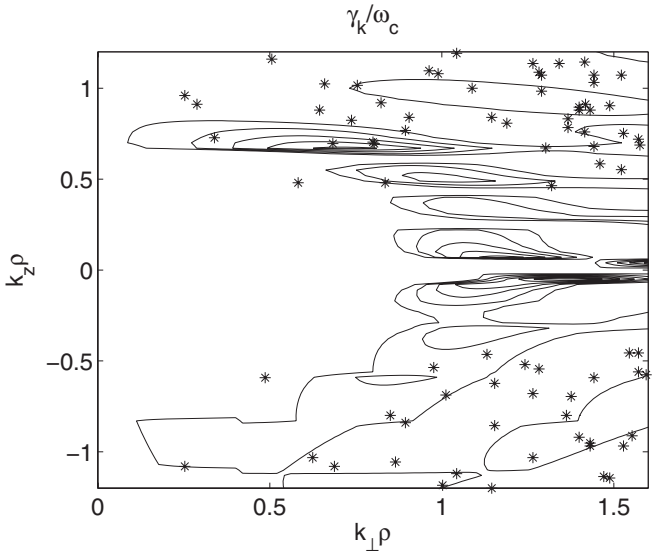

FIG. 9. Variation of the normalized growth rate γ_k/ω_c in the plane $(k_\perp\rho, k_z\rho)$, calculated using Eq. (1), for $\omega_p/\omega_c = 3$, $v_0 = 5$, $\theta_0 = 137^\circ$, $\sigma \simeq v_0/20$, $n_{res}/n_0 = 0.03$, $a = 1$, and $b = 0$. The regions of instability ($\gamma_k > 0$) are represented by isocontour lines. The stars indicate the parallel and perpendicular wave vectors of the 240 waves interacting with the horseshoe distribution. The figure shown is limited to the region $0 < k_\perp\rho < 1.6$ and $-1.2 < k_z\rho < 1.2$.

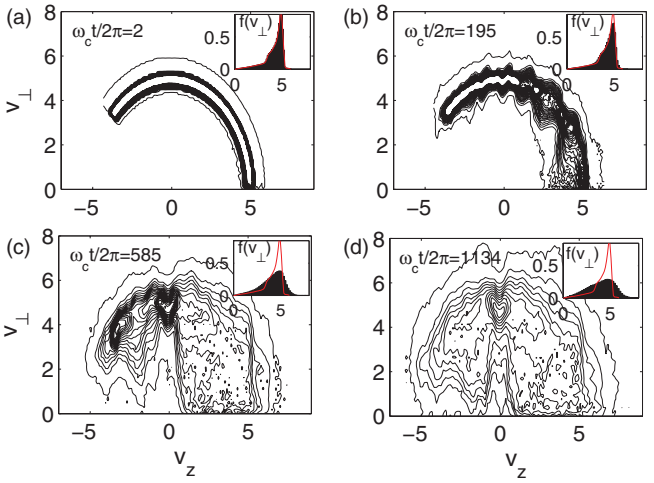

FIG. 10. (Color online) Isocontours of the horseshoe distribution in the plane $(v_z, v_\perp)$ for four moments of time (a) $\omega_c t/2\pi \simeq 2$, (b) $\omega_c t/2\pi \simeq 195$, (c) $\omega_c t/2\pi \simeq 585$, and (d) $\omega_c t/2\pi \simeq 1134$. The insets in each panel show, for the same time moments, the perpendicular velocity distribution $f(v_\perp)$ (black surface) superposed to its initial value [solid (red) line]. The parameters are the same as in Fig. 9.

work [27] and is confirmed by the present study. Below we discuss how the choice of the wave spectrum affects our results.

Several simulations with large numbers of waves and different distributions in **k** space have been done, the majority of them using the same hot electron distribution and plasma parameters. Let us first consider a spectrum of 240 waves whose wave vectors are more or less evenly and randomly distributed in the plane $(k_\perp\rho, k_z\rho)$, covering an area with several local instability maxima but, importantly, without including the region of instability at small $k_z\rho$ (see the growth rates and the localization of the selected waves in the region where instability is most important in Fig. 9). The evolution of the particle distribution in velocity space at four time points (see Fig. 10) shows that the development of the instability leads to the filling of the horseshoe by the particles, more quickly for the area with $v_z > 0$ than with $v_z < 0$. This is fully explained by the fact that the resonant particles interact with the most unstable waves, which have mostly positive k_z and whose growth rates are mainly due to the contributions of the $n = 0$ and 1 resonances (see also the above linear study and Fig. 9). However, the higher-order normal cyclotron resonances $n = 2$–5 of these waves are lying in the domain $-3 \lesssim v_z \lesssim 2$ and are responsible for the later and slower filling of the horseshoe in this region. As a result of the evolution, the perpendicular velocity distribution $f(v_\perp)$ is much wider and its asymptotic shape is characterized by a linear dependence at $v_\perp \lesssim v_0$ and a rather fast decay for $v_\perp > v_0$ [see the inset of Fig. 10(d)]. A redistribution of the particles' energy occurs, as some electrons ($\lesssim 30\%$) are accelerated in the perpendicular direction above v_0, reaching velocities $v_\perp^2 \geqslant 2v_0^2$. The asymptotic parallel distribution function $f(v_z)$ (not shown here) reveals that electrons are also accelerated along the magnetic field, but their number (a few percent) and the increase of their parallel velocities ($\Delta v_z/v_z \lesssim 20\%$) are not significant.

Figure 11(b) shows the time variation of the energy exchanges between waves and particles. In the early stage of the evolution ($\omega_c t/2\pi \lesssim 250$), the resonant particles transfer to the waves some part of their parallel and perpendicular energies, so $\mathcal{E}_z$ and $\mathcal{E}_\perp$ are decreasing (dotted and thin lines, respectively); note that the loss of parallel energy is more pronounced. Meanwhile, the total wave energy density W is growing (thick solid line) and saturating around $\omega_c t/2\pi \simeq 250$; then it slowly decreases up to $\omega_c t/2\pi \simeq 500$, showing that the waves begin to give back a part of their energy to the parallel motion of the particles, whereas they do not stop to extract energy from their perpendicular motion. The change of behavior of $\mathcal{E}_z$ after $\omega_c t/2\pi \simeq 250$ seems to be connected to the fact that for $\omega_c t/2\pi \lesssim 250$, interactions at the Landau and the normal cyclotron resonances ($n = 1$) are playing the main role, being able, in agreement with the corresponding invariant lines (10), to move particles to smaller v_z over larger Δv_z than the higher harmonics $n > 1$. Then, for $\omega_c t/2\pi \gtrsim 250$, the resonances $n > 1$ are mostly playing, which cannot decelerate particles as efficiently as $n = 0, 1$ along the parallel direction. Figure 11(a) completes the picture by presenting the time variation of the energy densities of the eight most unstable waves, which increase as expected, reaching a maximum near $\omega_c t/2\pi \simeq 200$–300 and then smoothly damping. Attenuation of the waves in the last stage of the evolution is easily explained; indeed, after the main relaxation of the particle distribution leading to the horseshoe filling, the instability disappears and its kinetic growth rate vanishes and becomes negative. However, one can observe that some waves reach their maximum only later near $\omega_c t/2\pi \simeq 800$ and even overcome the saturation levels of the others (the horseshoe filling not being finished at this stage), but all the waves are damped or saturated when the particle relaxation

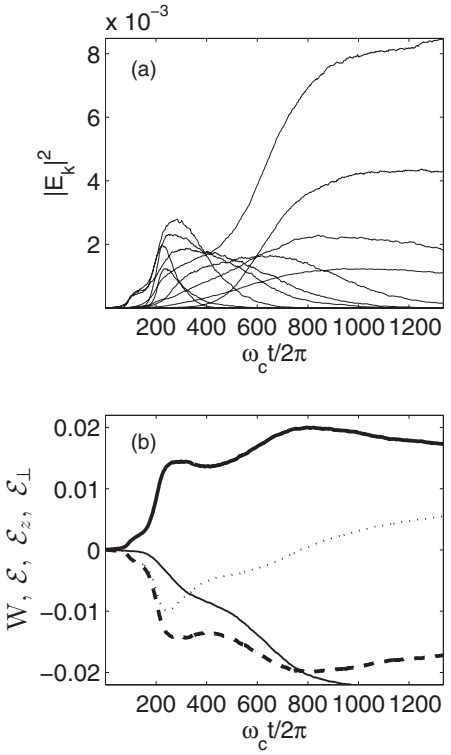

FIG. 11. (a)Variation with time $\omega_c t/2\pi$ of the normalized wave energy densities $W_k = |E_k|^2$ of the eight most unstable waves. (b) Corresponding time variation of the total wave energy density W (thick line) as well as the total (dashed line), the parallel (dotted line), and the perpendicular (thin line) kinetic energy densities of the particles, $\mathcal{E}$, $\mathcal{E}_z$, and $\mathcal{E}_\perp$, respectively, in arbitrary units. The parameters are the same as in Fig. 9.

is achieved, near $\omega_c t/2\pi \simeq 2500$. As already mentioned, the diffusion of the particles, leading to the filling of the horseshoe, occurs as a consequence of successive oscillations of the particles along the lines (10), with appropriate transitions from one invariant line to another. The motion of individual particles interacting resonantly with many waves shows the same features as those discussed when considering four waves. For illustration, Fig. 12, like Figs. 7 and 8, presents the projections of trajectories of several particles on the plane $(v_z, v_\perp)$. The particles with $4 \lesssim v_z \lesssim 6$ are mainly trapped at Landau and anomalous cyclotron resonances $n < 0$, following the corresponding invariant lines, with vanishing ($v_\perp \simeq \mathcal{C}$) or negative ($\Delta v_\perp/\Delta v_z = -|n|\omega_c/k_z v_\perp < 0$ for $k_z > 0$) slopes. The test electrons with $v_z \lesssim 4$ are mainly interacting with waves at normal cyclotron resonances $n > 0$, presenting complex motions such as those described above.

Let us compare the above results with a simulation performed with 500 waves (so-called S2), which differs from the previous one (so-called S1) only by the waves' distribution in **k** space. Note the important point that in S2 the wave vectors are distributed over the entire k_z region, including the domain where k_z is small and the instability growth rates γ_k are the largest (see Fig. 13, showing the localization of the waves and the regions of instability). The main features of the particle distribution's relaxation (Fig. 14) and the dynamics of the waves (Fig. 15) are similar in S2 and S1

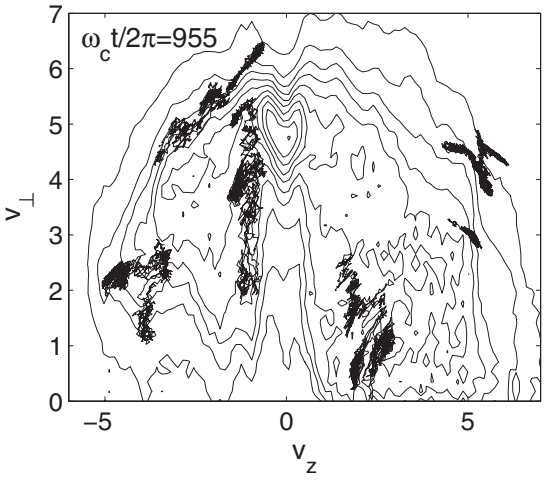

FIG. 12. Isocontours of the horseshoe distribution in the plane $(v_z, v_\perp)$ at $\omega_c t/2\pi \simeq 955$. The projections of several particle trajectories are superposed (see the black areas). The parameters are the same as in Fig. 9.

(see Figs. 10 and 11). However, several important differences exist. First, the development of the instability in S2 is much faster and, according to the linear theory, the waves with small k_z are the most rapidly growing. Second, the parallel velocity of the particles interacting with these waves almost does not vary during their oscillations along the invariant lines because ω_c/k_z is very large. Therefore, in the neighborhood of $v_z \simeq 2$ and -2 [see Fig. 14(b)], where the particles interact with these waves mainly at the second harmonics $n = 2$ of the normal cyclotron resonances, the particles' diffusion occurs along narrow vertical strips $v_z \simeq \mathcal{C}$ and the cases when particles transit from one resonance to another are rare. It is also worth noting the markedly pronounced

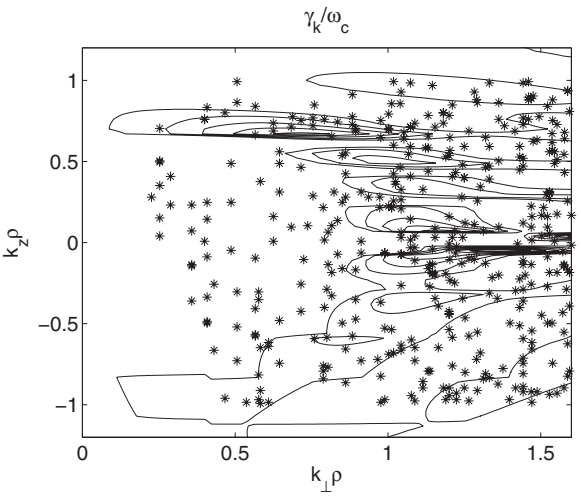

FIG. 13. Variation of the normalized growth rate γ_k/ω_c in the plane $(k_\perp\rho, k_z\rho)$, calculated using Eq. (1), for the parameters $\omega_p/\omega_c = 3$, $v_0 = 5$, $\theta_0 = 137^\circ$, $\sigma \simeq v_0/20$, $n_{res}/n_0 = 0.03$, $a = 1$, and $b = 0$. The regions of instability ($\gamma_k > 0$) are represented by isocontour lines. The stars indicate the parallel and perpendicular wave vectors of the 500 waves interacting with the horseshoe distribution. The figure is limited to the region $0 < k_\perp\rho < 1.6$ and $-1.2 < k_z\rho < 1.2$.

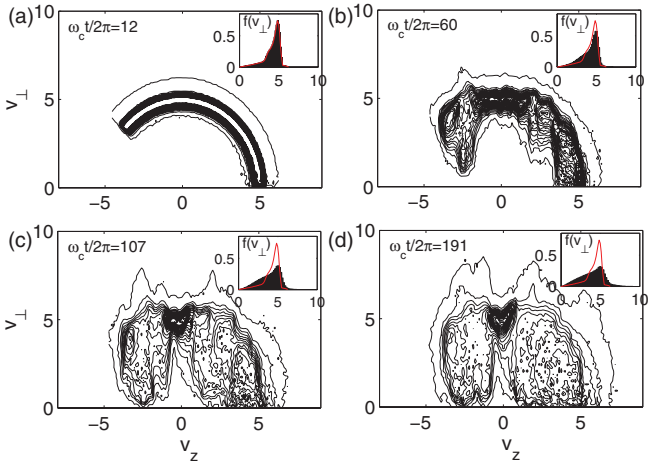

FIG. 14. (Color online) Isocontours of the horseshoe distribution in the plane $(v_z, v_\perp)$ for four moments of time (a) $\omega_c t/2\pi \simeq 12$, (b) $\omega_c t/2\pi \simeq 60$, (c) $\omega_c t/2\pi \simeq 107$, and (d) $\omega_c t/2\pi \simeq 191$. The insets in each panel show, for the same time moments, the perpendicular velocity distribution $f(v_\perp)$ (black surface) superposed to its initial value [solid (red) line]. The parameters are the same as in Fig. 13.

perpendicular acceleration of particles near $v_z \simeq 2$ and -2 [Fig. 14(d)]. The third difference of S1 is that, during the whole process, the energy exchanges mainly occur between the waves

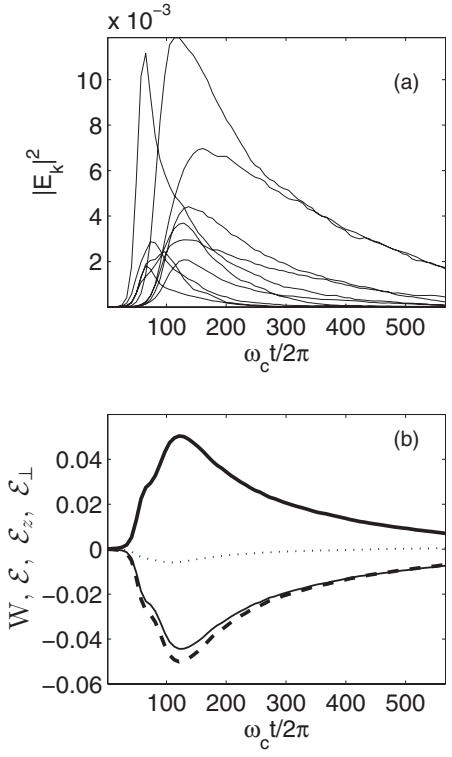

FIG. 15. (a)Variation with time $\omega_c t/2\pi$ of the normalized wave energy densities $W_k = |E_k|^2$ of the eight most unstable waves. (b) Corresponding time variation of the total wave energy density W (thick line) as well as the total (dashed line), the parallel (dotted line), and the perpendicular (thin line) kinetic energy densities of the particles, $\mathcal{E}, \mathcal{E}_z$, and $\mathcal{E}_\perp$, respectively, in arbitrary units. The parameters are the same as in Fig. 13.

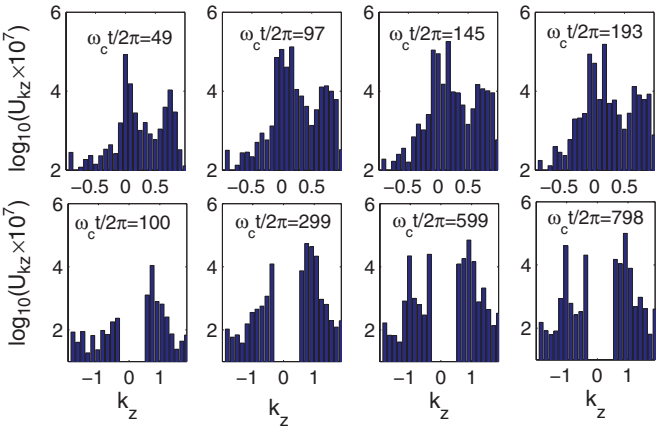

FIG. 16. (Color online) Averaged wave spectra: wave energy density $U_{k_z} = \sum_{k_z - \Delta k_z \leqslant k'_z < k_z} |E_{k'}|^2$ [in logarithmic units and black (blue) bars] as a function of k_z for the waves' distribution of Figs. 13–15 including waves with small k_z (upper row, simulation S2) and the waves' distribution of Figs. 9– 12 excluding the waves with large parallel wavelengths (bottom row, simulation S1). The spectra are shown at four moments of time (upper row, from left to right) $\omega_c t/2\pi \simeq 49, 97, 145, 193$ and (bottom row, from left to right) $\omega_c t/2\pi \simeq 100, 299, 599, 798$.

and the perpendicular motion of the particles [see Fig. 15(b)]. The variation of kinetic energy along the magnetic field is small, in particular in the initial stage of the waves' growth and during the process of wave attenuation in the final stages of the relaxation. Fourth, the maximum of the total wave energy density in S2 is 2.5 times larger than that in S1. Moreover, let us compare the evolution of the wave spectra by analyzing the energy density $U_{k_z} = \sum_{k_z - \Delta k_z \leqslant k'_z < k_z} |E_{k'}|^2$ of all waves whose k_z lies in a given interval Δk_z (i.e., averaged over $k_\perp$). Figure 16 shows the averaged wave spectra U_{k_z} obtained for S1 and S2 at four moments of time. One can see that for S2 (upper row) the waves with large parallel wavelengths k_z^{-1} dominate during the entire process, although the spectrum exhibits a noticeable short-wavelength component. In S1 the long waves are removed artificially, although one observes that at the time when the total wave energy W is maximum (i.e., near $\omega_c t/2\pi \simeq 97$ for S2 and $\omega_c t/2\pi \simeq 798$ for S1), the amplitudes of the short waves are similar in both cases. In conclusion, the inclusion of waves with small k_z leads to significant quantitative differences in the relaxation rate of the distribution during the first stage of the evolution as well as in the magnitude of the maximum wave energy reached due to instability. However, from a qualitative point of view and as a whole, waves and particles behave similarly in both simulations S1 and S2.

As observed above, the filling of the horseshoe in the region $v_z < 0$ is slower than in the region $v_z > 0$; this effect is even more pronounced if the horseshoe distribution presents a strong asymmetry, i.e., a decrease, in phase space, of the particle density with v_z. Let us now consider such a distribution interacting with the waves' set of S1. First, a linear instability analysis shows that the parallel wave numbers k_z of the most excited waves are positive. Indeed, as the waves interact more strongly with particles in the velocity regions where the local electron density is larger (i.e., at $v_z > 0$) (the growth rate being

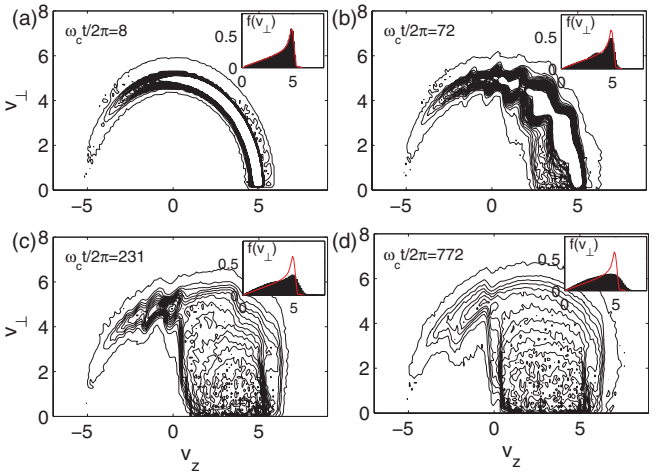

FIG. 17. (Color online) Horseshoe with varying density: isocontours of the distribution in the plane $(v_z, v_\perp)$ for four moments of time (a) $\omega_c t/2\pi \simeq 8$, (b) $\omega_c t/2\pi \simeq 72$, (c) $\omega_c t/2\pi \simeq 231$, and (d) $\omega_c t/2\pi \simeq 772$. The insets in each panel show, for the same time moments, the perpendicular velocity distribution $f(v_\perp)$ (black surface) superposed to its initial value [solid (red) line]. The parameters are $\omega_p/\omega_c = 3$, $v_0 = 5$, $\theta_0 = 137^\circ$, $\sigma \simeq v_0/20$, $n_{res}/n_0 = 0.03$, $a = 1$, and $b = 1$.

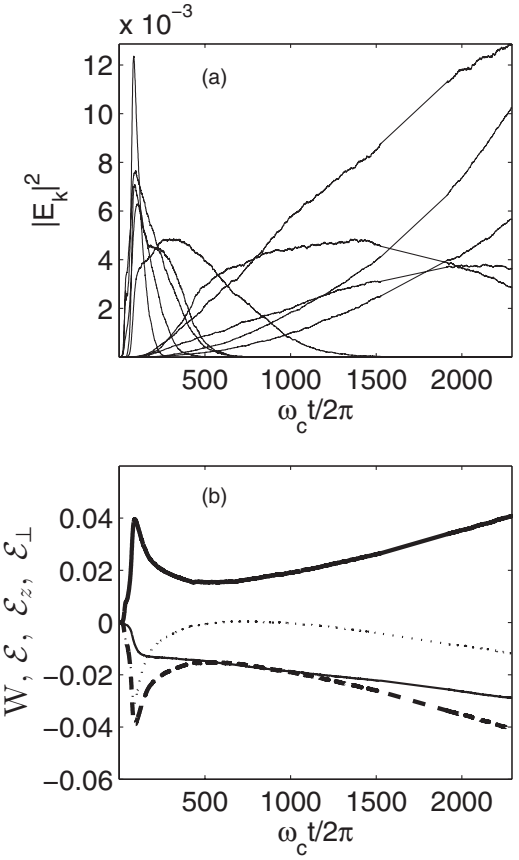

FIG. 18. Horseshoe with varying density: (a) variation with time $\omega_c t/2\pi$ of the normalized wave energy densities $W_k = |E_k|^2$ of the eight most unstable waves and (b) corresponding time variation of the total wave energy density W (thick line) as well as the total (dashed line), the parallel (dotted line), and the perpendicular (thin line) kinetic energy densities of the particles, $\mathcal{E}$, $\mathcal{E}_z$, and $\mathcal{E}_\perp$, respectively, in arbitrary units. The parameters are the same as in Fig. 17.

proportional to the density) and as the fundamental resonances $n = 0, 1$ contribute mainly to the wave growth when no small k_z are present (see above), the resonant velocities v_{z0}, v_{z1} of the most excited waves are positive and thus also are their parallel wave numbers. Then, in the region $v_z < 0$, the particles' oscillations in wave fields are very small. Moreover, the modification of the particle distribution in the nonlinear stage of the evolution is also weak. Figure 17 shows the horseshoe at four moments of time during the relaxation process. One observes that for $v_z > 0$ the relaxation occurs similarly to the cases S1 and S2 considered above, which present more symmetric distributions. As noted previously, the anomalous cyclotron resonances play no significant role here.

Similarly to the previous cases, the instability development reveals two stages (Fig. 18). First, for $\omega_c t/2\pi \lesssim 100$, the wave energy grows rapidly, whereas the distribution is strongly modified and the particles only give energy to the waves, with no counterpart (monotonic decreasing of $\mathcal{E}_z$ and $\mathcal{E}_\perp$). The faster (compared to S1) wave energy growth is easily explained by the larger growth rates of the most unstable waves (with $k_\perp \lesssim 1.5$ and $k_z \simeq 0.7$) due to the increased number of particles at $v_z > 0$ in the asymmetric case while maintaining the total density n_{res}/n_0 of the hot particles constant. The greater magnitude of the growth rate γ_k also allows us to explain the larger wave energy maximum $W_{\max}$ if we observe that, in the growth stage, a small number of waves dominate and, according to the calculations with one wave, their energy at saturation increases as $|E_k|^2 \sim \gamma_k^\alpha$ (where $\alpha > 1$ and, in the case of a single wave, $\alpha \simeq 3$). The second stage ($100 \lesssim \omega_c t/2\pi \lesssim 500$) is characterized by a slow decay of the wave energy, which is spent to increase the parallel kinetic energy [Fig. 18(b)]. In almost the whole $(v_z, v_\perp)$ plane, the horseshoe relaxes slowly to its asymptotic state and experiences only small adjustments during the second stage (Fig. 17). However, besides this two-stage relaxation, the simulation shows a somewhat different feature of energy exchange between waves and particles: A slow growth of wave energy density occurs during a third stage, when $\omega_c t/2\pi \gtrsim 500$ (see Fig. 18). In this case, the energy of the waves is mainly transferred to the parallel motion of the electrons. This effect is conditioned by the rest of the free particle energy associated with the formation of a positive gradient $\frac{\partial}{\partial v_z} \int f(v_z, v_\perp) d(\pi v_\perp^2) > 0$ in the parallel velocity distribution at $v_z \lesssim 2.5$ (not shown here). In the previous simulations involving more symmetric initial velocity distributions, such an effect also occurred, but for a limited time and with a much smaller magnitude. Moreover, a more detailed analysis shows that the growth is observed only for the waves with a Landau resonant velocity $v_{z0} = \omega_k/k_z \lesssim 2.5$. Because this effect occurs in a velocity range close to the thermal velocity, any further calculation can be meaningful only if one takes into account the wave damping due to the thermal bulk, which is not included in our model; however, in spite of that, we can assume that the third stage of relaxation is brief or absent and does not have a significant impact on the established distribution of hot particles.

IV. CONCLUSION

Numerical simulations have shown that low-energy and low-density horseshoe or shell-type electron distributions can generate high-frequency waves of finite amplitudes propagating obliquely to the ambient magnetic field, in agreement with space observations. The dynamics of wave packets interacting with horseshoe-type distributions, which was investigated using a symplectic code based on a three-dimensional Hamiltonian model, was shown to be mainly governed not only by interactions occurring at Landau $n = 0$ and normal $n = 1$ cyclotron resonances, but also at higher-order harmonics $n > 1$, which play an essential and determinant role.

Simulations performed with a limited number of waves reveal some specific features of the motion of the particles interacting simultaneously with several waves at multiple resonances of different natures and orders, showing that such complex processes determine the main features of the evolution of the waves' spectrum. Simulations with wave packets presenting quasicontinuous spectra provide a full picture of the relaxation of the horseshoe distribution, revealing two main phases of the evolution: an initial stage of wave energy growth, characterized by a fast filling of the shell, and a second phase of slow damping of the wave energy, accompanied by final adjustments of the horseshoe distribution. Moreover, the influence of density inhomogeneity along the shell modifies quantitatively the energy exchanges between the waves and the particles due to the strong asymmetry of the horseshoe distribution interacting resonantly with the wave packet.

Finally, note that the instability growth rates have been determined using the linear theory as a function of the opening angle, the velocity, and the relative thickness of the horseshoe, as well as of the ratio of the plasma to the cyclotron frequency and the interaction resonance.

The question arises as to how the nonlinear phenomena described in the present paper can influence the generation of horseshoe distributions. In principle, as soon as a positive perpendicular gradient appears in the distribution function formed by the penetration of an electron beam in a inhomogeneous magnetic field and as soon as this distribution under formation presents a large enough opening angle (roughly $\theta_0 \gtrsim 30^\circ$), an instability can develop that widens the shell, thus reducing the instability growth rates. Thus it will be a competition between the two following processes occurring on different time scales: the process of beam penetration in the magnetic field and the widening of the horseshoe due to instability and wave emission. If the second process is faster than the first one, the instability and further nonlinear effects can act to limit the wave growth by widening the shell, which can be partially or totally filled eventually; then the resulting distribution may or may not contain some remaining free energy in the form of a positive perpendicular gradient. Otherwise, it is likely that the processes described in the present paper will occur when the horseshoe is fully formed; our paper offers the possibility to model such situations.

ACKNOWLEDGMENTS

The authors acknowledge the Centre National de la Recherche Scientifique (France), the Ecole Polytechnique (France), the Russian Academy of Sciences, and the Russian Foundation for Fundamental Research (Grant No. 09-02-91052) for their financial support. The authors acknowledge Dr. Marie Flé (Direction Informatique, Université Paris–Sud, Orsay) for her technical support.

APPENDIX: NONLINEAR MODEL OF RESONANT WAVE-PARTICLE INTERACTIONS

A Hamiltonian self-consistent wave-particle model has been developed in order to study the nonlinear interaction of a packet of electrostatic waves with a nonequilibrium particle distribution in a magnetized plasma. It is supposed that the plasma electrons can be divided into two groups: (i) the nonresonant thermal bulk, i.e., the ambient plasma supporting the wave dispersion, and (ii) the so-called resonant electrons forming the horseshoe, which interact strongly with the waves at different resonance conditions and whose density is much smaller than that of the ambient plasma $n_{res}/n_0 \ll 1$. The thermal component determines the waves' dispersion and is described in the linear approximation using hydrodynamic equations. However, the resonant particles have to be considered owing to a kinetic approach that takes into account their full nonlinear dynamics in the waves' fields.

The system is supposed to be periodic in space. For electrostatic oscillations in a homogeneous magnetized plasma, the electric field $\mathbf{E}$ is derived from the scalar potential $\varphi = \mathrm{Re}(\sum_{\mathbf{k}} \varphi_{\mathbf{k}} e^{i\mathbf{k}\cdot\mathbf{r} - i\omega_{\mathbf{k}} t})$, which consists in the superposition of plane waves with slowly varying amplitudes $\varphi_{\mathbf{k}}(t)$, so the average electric field energy density of the wave with frequency $\omega_{\mathbf{k}}$ and wave vector $\mathbf{k}$ is given by $\langle E_{\mathbf{k}}^2/8\pi \rangle = |\mathbf{k}\varphi_{\mathbf{k}}|^2/16\pi$. In a plasma with constant ambient magnetic field $\mathbf{B}_0 = B_0\mathbf{z}$, the motion of a particle p in the waves' electric field $\mathbf{E} = -\nabla\varphi$ is described by the Newton equations (e and m_e are the electron charge and mass)

$$\frac{d\mathbf{v}_p}{dt} + \frac{e}{m_e c}\mathbf{v}_p \times \mathbf{B}_0 = \frac{e}{m_e}\,\mathrm{Re}\sum_{\mathbf{k}} i\mathbf{k}\varphi_{\mathbf{k}} e^{i\eta_p}, \tag{A1}$$

which can be presented in the Hamiltonian form as $d\mathbf{P}_p/dt = -\partial H_0/\partial \mathbf{r}_p$, with $d\mathbf{r}_p/dt = \partial H_0/\partial \mathbf{P}_p = \mathbf{v}_p$, where $\mathbf{P}_p = m_e\mathbf{v}_p - e\mathbf{A}_0(\mathbf{r}_p)/c$ is the generalized particle momentum, $\mathbf{r}_p(\mathbf{r}_{\perp p}, z_p)$ and $\mathbf{v}_p(\mathbf{v}_{\perp p}, v_{zp})$ are the particle's position and velocity; $\eta_p = \mathbf{k}\cdot\mathbf{r}_p - \omega_{\mathbf{k}} t$ is the phase of the particle p located at the position $\mathbf{r}_p$, and $\mathbf{A}_0(\mathbf{r}_p) = (\mathbf{B}_0 \times \mathbf{r}_p)/2$ is the vector potential. The corresponding Hamiltonian is

$$H_0 = \sum_p \left(\frac{[\mathbf{P}_p + e\mathbf{A}_0(\mathbf{r}_p)/c]^2}{2m_e} - e\,\mathrm{Re}\sum_{\mathbf{k}} \varphi_{\mathbf{k}} e^{i\eta_p} \right). \tag{A2}$$

Note that in the absence of wave-wave interactions, the full Hamiltonian should include the wave energy $\sum_{\mathbf{k}} \omega_{\mathbf{k}} |C_{\mathbf{k}}|^2$ expressed through the normal wave amplitudes $C_{\mathbf{k}}(t) \propto \varphi_{\mathbf{k}}(t) e^{-i\omega_{\mathbf{k}} t}$ as

$$\sum_{\mathbf{k}} \omega_{\mathbf{k}} |C_{\mathbf{k}}|^2 = V \sum_{\mathbf{k}} W_{\mathbf{k}} = V \sum_{\mathbf{k}} \omega_{\mathbf{k}} \frac{\partial \varepsilon_{\mathbf{k}}}{\partial \omega_{\mathbf{k}}} \frac{|\mathbf{k}\varphi_{\mathbf{k}}|^2}{16\pi}, \tag{A3}$$

where $\sum_{\mathbf{k}} W_{\mathbf{k}}$ is the energy density of the electrostatic waves in a unit volume and $\varepsilon_{\mathbf{k}}$ is the plasma dielectric function; V is the volume occupied by the wave-particle system. From above

follows the relationship between the normal wave amplitudes $C_{\mathbf{k}}$ and their electric potential $\varphi_{\mathbf{k}}$,

$$C_{\mathbf{k}}(t) = \sqrt{\frac{\mathbf{k}^2 V}{16\pi}\frac{\partial \varepsilon_{\mathbf{k}}}{\partial \omega_{\mathbf{k}}}}\varphi_{\mathbf{k}}(t)e^{-i\omega_{\mathbf{k}}t}. \tag{A4}$$

The equation describing the time evolution of the wave amplitudes can be obtained from the full Hamiltonian

$$H = H_0 + \sum_{\mathbf{k}} \omega_{\mathbf{k}} |C_{\mathbf{k}}|^2 \tag{A5}$$

according to

$$\frac{\partial C_{\mathbf{k}}}{\partial t} = -i\frac{\partial H}{\partial C^*_{\mathbf{k}}} = -i\omega_{\mathbf{k}} C_{\mathbf{k}} + i\frac{e}{2}\frac{\partial \varphi^*_{\mathbf{k}}}{\partial C^*_{\mathbf{k}}}\sum_p e^{-i\eta_p}. \tag{A6}$$

Thus, using Eq. (A4) we get

$$\frac{\partial}{\partial t}\frac{e\varphi_{\mathbf{k}}}{m_e} = \frac{2i\omega_p^2}{\mathbf{k}^2\frac{\partial \varepsilon_{\mathbf{k}}}{\partial \omega_{\mathbf{k}}}}\frac{n_{res}}{n_0}\frac{1}{N}\sum_p e^{-i\eta_p}, \tag{A7}$$

where N is the number of resonant particles of density n_{res} inside the volume V, $N = n_{res}V$. The Hamiltonian structure ensures the conservation of the total energy H and momentum P_z,

$$H = \mathcal{C}, \quad P_z = \sum_p m_e v_{zp} + V\sum_{\mathbf{k}}\frac{k_z}{\omega_{\mathbf{k}}}W_{\mathbf{k}} = \mathcal{C}. \tag{A8}$$

For upper-hybrid waves with $\omega_{\mathbf{k}} \gg \omega_c$, the approximate dispersion relation is given by Eq. (4) and $\partial\varepsilon_{\mathbf{k}}/\partial\omega_{\mathbf{k}} \simeq 2/\omega_{\mathbf{k}}$, so we get the equation of wave evolution in the form

$$\frac{\partial}{\partial t}\frac{e\varphi_{\mathbf{k}}}{m_e} = i\frac{\omega_p^2\omega_{\mathbf{k}}}{\mathbf{k}^2}\frac{n_{res}}{n_0}\frac{1}{N}\sum_p e^{-i\eta_p}. \tag{A9}$$

The model allows us to choose arbitrary sets of waves $(\mathbf{k},\omega_{\mathbf{k}})$ for which the periodicity conditions have to be verified, i.e., $k_{x,y,z}L_{x,y,z}/2\pi = \pm 1, \pm 2, \ldots$, where $[L_x, L_y, L_z]$ is a three-dimensional spatial simulation box of volume $V = L_xL_yL_z$. The initial velocity distribution of the resonant electrons is modeled by the function (8). Initially all resonant particles are randomly distributed within the box $[L_x, L_y, L_z]$ with the same probability to occupy any position in the volume V.

Owing to the Hamiltonian structure of the model, the numerical simulations are performed using a symplectic mover with time steps $\omega_c\Delta t \simeq 0.1$–$0.2$ while checking the accuracy of the calculations with the help of the H and P_z conservations (A8). As one can separate the Hamiltonian (A5) as $H = H_1 + H_2$, where $H_1 = \sum_{p=1}^{N}(\mathbf{P}_p + e\mathbf{A_0}/c)^2/2m_e$, the symplectic operator $L(\Delta t) = L_1(\Delta t/2)L_2(\Delta t)L_1(\Delta t/2) + o(\Delta t^3)$ of order 2 in time step can be used for advancing the Hamiltonian H (L_1 and L_2 are canonical transformations applying to H_1 and H_2, respectively). More technical details are given in Ref. [25].

[1] L. Eliasson, M. André, A. Eriksson, P. Norqvist, O. Norberg, R. Lundin, B. Holback, H. Koskinen, H. Borg, and M. Boehm, Geophys. Res. Lett. **21**, 1911 (1994).

[2] A. Roux, A. Hilgers, H. de Feraudy, D. Le Queau, P. Louarn, S. Perraut, A. Bahnsen, M. Jespersen, E. Ungstrup, and M. André, J. Geophys. Res. **98**, 11657 (1993).

[3] R. Bingham, B. J. Kellett, R. A. Cairns, R. O. Dendy, and P. K. Shukla, Geophys. Res. Lett. **26**, 2713 (1999).

[4] G. T. Delory, R. E. Ergun, C. W. Carlson, L. Muschietti, C. C. Chaston, W. Peria, J. P. McFadden, and R. Strangeway, Geophys. Res. Lett. **25**, 2041 (1998).

[5] D. Bryant, *Electron Acceleration in the Aurora and Beyond* (IOP, Bristol, 1999).

[6] R. E. Ergun, C. W. Carlson, J. P. McFadden, G. T. Delory, R. J. Strangeway, and P. L. Pritchett, Astrophys. J. **538**, 456 (2000).

[7] J. M. Urrutia and R. L. Stenzel, J. Geophys. Res. **88**, 7086 (1983).

[8] D. Speirs, I. Vorgul, K. Ronald, R. Bingham, R. Cairns, A. Phelps, B. Kellett, A. Cross, C. Whyte, and C. Robertson, J. Plasma Phys. **71**, 665 (2005).

[9] R. Bingham and R. A. Cairns, Phys. Scr. **T98**, 160 (2002).

[10] R. Bingham, B. J. Kellett, R. A. Cairns, J. Tonge, and J. T. Mendonega, Astrophys. J. **595**, 279 (2003).

[11] R. A. Treumann, Astron. Astrophys. Rev. **13**, 229 (2006).

[12] P. Pritchett, R. Strangeway, C. Carlson, R. Ergun, J. McFadden, and G. Delory, J. Geophys. Res. **104**(A5), 10317 (1999).

[13] D. Sundkvist, A. Vaivads, Y. V. Bogdanova, V. V. Krasnoselskikh, A. Fazakerley, and P. M. E. Decreau, Geophys. Res. Lett. **33**, L03103 (2006).

[14] W. S. Kurth, L. A. Frank, M. Ashour-Abdalla, D. A. Gurnett, and B. G. Burek, Geophys. Res. Lett. **7**, 293 (1980).

[15] D. D. Sentman, J. N. Leboeuf, T. Katsouleas, R. W. Hu, and J. Dawson, Phys. Fluids **29**, 2569 (1986).

[16] R. Dory, G. Guest, and E. Harris, Phys. Rev. Lett. **14**, 131 (1965).

[17] L. D. Pearlstein, M. N. Rosenbluth, and D. B. Chang, Phys. Fluids **9**, 953 (1966).

[18] A. Mikhailovskii, *Theory of Plasma Instabilities. 1. The Instabilities of Homogeneous Plasma* (Atomizdat, Moscow, 1975).

[19] R. Bingham and R. A. Cairns, Phys. Plasmas **7**, 3089 (2000).

[20] A. Volokitin and C. Krafft, Phys. Plasmas **11**, 3165 (2004).

[21] A. Zaslavsky, C. Krafft, and A. Volokitin, Phys. Plasmas **14**, 122302 (2007).

[22] C. Krafft, A. Volokitin, and A. Zaslavsky, Phys. Rev. E **82**, 066402 (2010).

[23] A. B. Kitsenko, I. M. Pankratov, and K. N. Stepanov, Plasma Phys. **17**, 173 (1975).

[24] C. Krafft, A. Volokitin, and A. Zaslavsky, Phys. Plasmas **12**, 112309 (2005).

[25] A. Zaslavsky, C. Krafft, and A. Volokitin, Phys. Rev. E **73**, 016406 (2006).

[26] A. Volokitin and C. Krafft, Plasma Phys. Control. Fusion **54**, 085002 (2012).

[27] C. Krafft and A. Volokitin, Phys. Plasmas **13**, 122301 (2006).